Urbonas, Darius; Moilanen, Antti J.; Arnardottir, Kristin B.; Scherf, Ullrich; Mahrt, Rainer F.; Törmä, Päivi; Stöferle, Thilo

Temporal mode switching during polariton condensation

Published in:
Communications Physics

DOI:
10.1038/s42005-024-01667-w

Published: 01/12/2024

Document Version
Publisher's PDF, also known as Version of record

communications physics

Article

https://doi.org/10.1038/s42005-024-01667-w

Temporal mode switching during polariton condensation

Darius Urbonas [1,8] ✉, Antti J. Moilanen [2,3,8] ✉, Kristin B. Arnardottir [4,5,6], Ullrich Scherf [7], Rainer F. Mahrt [1], Päivi Törmä [2] & Thilo Stöferle [1]

Multimode behavior plays a key role in a wide range of nonlinear optical phenomena. Multiple exciton-polariton modes can attain macroscopic population as observed in time-integrated measurements. Recent theory work has shown that, rather than being simultaneously in many modes, the population may temporally switch between the modes. However, the origin and the dynamics of multimode condensation has not been experimentally addressed. Here, we study the dynamics of exciton-polariton condensation into multiple modes of Gaussian defect microcavities filled with ladder type polymer gain material methyl-substituted ladder-type poly(p-phenylene) MeLPPP. We deploy a second-order cumulant model to simulate the dynamics of the system and find picosecond-timescale switching between condensate modes. By interferometric measurements we reveal the experimental signatures of such mode competition behaviour.

Strong coupling between photons and excitons gives rise to hybrid light-matter quasiparticles in a microcavity, called exciton-polaritons ("polaritons"). The polaritons' effective mass is dominated by the light mass of the photon, enabling non-equilibrium Bose-Einstein condensation (BEC)[1–3] even at room temperature[4–6]. Importantly, polaritons can interact directly (e.g. Coulombic) or indirectly (phase-space filling) via their matter component, which is important for all-optical device platforms, wherein the lack of sizable interactions between photons is a fundamental limitation[7]. Polariton condensates have already demonstrated potential for a variety of all-optical applications such as polariton amplifiers[8, 9], transistors[10], switches[11, 12], and phase modulators[13], with some of them working in non-cryogenic settings[14], as well.

All-optical switching is of particular interest for many applications such as communication and optical computing, and various approaches have been investigated[15]. All-optical switching and modulation have primarily been achieved through manipulation of the refractive index[16]. Ultrafast switching of a polarization state has been demonstrated in hybrid chiral dielectric-plasmonic resonators[17] and with epsilon-near-zero material coupled to plasmonic nanoantenna arrays[18]. Moreover, switching between different spatial modes of a polariton condensate has been reported in a few systems, including an annular trap[19], an elliptically shaped two-dimensional potential[20], and a multi-beam spatially patterned potential[21].

In general, although multimode polariton lasing/condensation with well-defined, discrete states has been reported[22, 23], the origin and the dynamics of multimode condensation has not been experimentally addressed before. A key question is whether the multiple condensates originate from a condensate that is *simultaneously* present in many modes, or if the polariton population re-distributes between the modes temporally, resulting in multiple peaks in time-integrated spectra.

It was recently proposed theoretically that multiple polariton lasing peaks in time-integrated photoluminescence spectra of organic microcavities may arise from temporal mode switching[24, 25]. In strongly coupled systems, the mode competition was explained by pump-induced shifts in polariton mode energies and the gain spectrum.

Here, we present experimental signatures of such mode competition in a tunable Gaussian double-defect microcavity filled with emissive polymer in the strong light-matter interaction regime. Tuning the microcavity length allows us to select three modes in the cavity and form polariton condensates in the 1st, 2nd, and 3rd localized states of the double-defect microcavity at room temperature[26]. In order not to be limited by the time-resolution of a streak camera or other detectors, we choose instead an interferometric correlation method. Using a Michelson interferometer, we measure the first-order coherence of localized states as a function of delay between the two interferometer arms. This allows us to study switching dynamics

[1]IBM Research–Zürich, Rüschlikon, Switzerland. [2]Department of Applied Physics, Aalto University School of Science, Aalto, Finland. [3]Photonics Laboratory, ETH Zürich, Zürich, Switzerland. [4]DTU Fotonik, Technical University of Denmark, Kongens Lyngby, Denmark. [5]NanoPhoton-Center for Nanophotonics, Technical University of Denmark, Kongens Lyngby, Denmark. [6]SUPA, School of Physics and Astronomy, University of St Andrews, St Andrews, United Kingdom. [7]Macromolecular Chemistry Group and Institute for Polymer Technology, Bergische Universität Wuppertal, Wuppertal, Germany. [8]These authors contributed equally: Darius Urbonas, Antti J. Moilanen. ✉e-mail: dar@zurich.ibm.com; amoilanen@ethz.ch

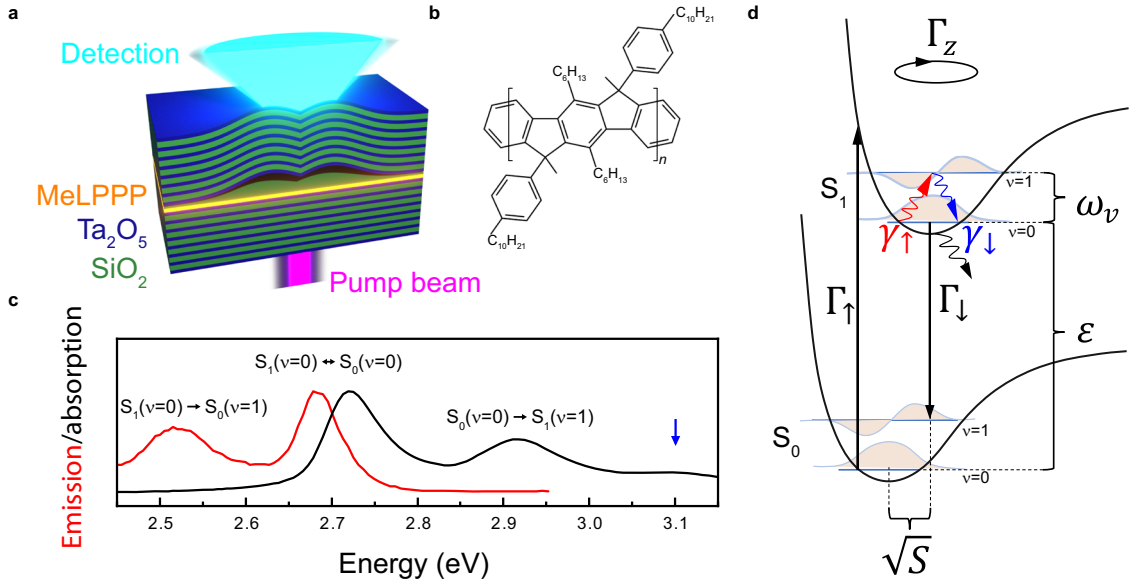

Fig. 1 | Schematic of experimental system. Microcavity filled with ladder-type conjugated polymer MeLPPP. **a** Sketch of the fabricated double-defect cavity. **b** Chemical structure of the MeLPPP polymer. **c** Measured absorption and emission spectra of MeLPPP. **d** Two-level system with both ground (S_0) and excited state (S_1) dressed by vibrational states. The bare transition energy between the two electronic states is denoted by ϵ, the vibrational frequency by ω_v, and the Huang-Rhys factor by S. The rates of the drive and dissipation processes involved are the external pumping $\Gamma_\uparrow$, spontaneous decay $\Gamma_\downarrow$, dephasing Γ_z, and thermal excitation and dissipation of the vibrational modes $\gamma_{\uparrow,\downarrow}$.

between polariton condensate modes at ambient conditions. Extracting the interference fringe amplitude, we observe oscillations due to temporal mode competition.

Results and discussion

We fabricate optical cavities realizing a Gaussian-shaped double-well (Fig. 1a) filled with an optically active polymer (Fig. 1b, c) in a strong light-matter interaction regime (see "Methods" section for more details). Fitting the observed polariton branches to a coupled oscillator model we obtain a light-matter coupling strength of $2\Omega = 120$–130 meV (see Supplementary Notes 1 and 2 and Supplementary Figs. 1 and 2 for the cavity dispersion and coupled oscillator fits).

Polariton condensation in a Gaussian double-well microcavity

First, we drive the system into the polariton condensation regime by optically exciting with a pulsed amplified laser source with 400 nm excitation wavelength and 2–4 ps pulse duration (see "Methods" section). By tuning the cavity length using nanopositioning stages (see "Methods" section) we reach a regime where we observe seemingly simultaneous condensation in three modes of the microcavity (Fig. 2). To identify the characteristic real-space mode profile, we investigate the spatial distribution of polaritons in the double-well microcavity. We select the emission from different modes by using a 5 meV-narrow, tunable spectral filter, and a polarizer. The filtered real-space images of condensates in the $k = 1, 2, 3$ localized states are shown in Fig. 2a, respectively. The three modes are clearly visible, and the patterns match the ones observed below threshold[26]. Above the condensation threshold, the emission intensity of the three modes increases non-linearly, Fig. 2b. The modes exhibit slightly different thresholds and their input-output curves, where we plot the emission versus the excitation fluence, cross. Importantly, above threshold multiple modes attain macroscopic population.

Simulations of mode populations

To study the dynamics behind multi-modal polariton condensation, we simulate the time-evolution of the system by a second-order cumulant model[24,25]. The system comprises N_m vibrationally dressed two-level emitters dispersed randomly in an optical microcavity that hosts multiple discrete photon modes. The optical cavity modes are strongly coupled to the electronic states of the emitters.

The coupled system is modeled by the Tavis–Cummings–Holstein Hamiltonian under the rotating wave approximation[24,27,28]:

$$H = \sum_k \omega_k a_k^\dagger a_k + \sum_{n,k}\left(g_{n,k} a_k \sigma_n^+ + g_{n,k}^* a_k^\dagger \sigma_n^-\right) + \sum_n \left[\frac{\varepsilon}{2}\sigma_n^z + \omega_v\left(b_n^\dagger b_n + \sqrt{S}\left(b_n^\dagger + b_n\right)\sigma_n^z\right)\right]. \quad (1)$$

Here $a_k^\dagger$ is the creation operator of cavity photon mode k, $\sigma_n^{z,+,-}$ are the Pauli operators of electronic states of emitter n, and $b_n^\dagger$ is the creation operator of vibrational excitation on emitter n. The energies of cavity photons and vibrational excitations are ω_k and ω_v, respectively. The transition energy of the emitters is ε.

Drive and dissipation processes are taken into account by the Lindblad formalism, which leads to the following equation of motion for the system density operator

$$\partial_t \rho = -i[H,\rho] + \sum_k \kappa_k \mathcal{L}[a_k] + \sum_n \Big(\Gamma_\uparrow P(t)\mathcal{L}[\sigma_n^+] + \Gamma_\downarrow \mathcal{L}[\sigma_n^-] + \Gamma_z \mathcal{L}[\sigma_n^z] + \gamma_\uparrow \mathcal{L}[b_n^\dagger + \sqrt{S}\sigma_n^z] + \gamma_\downarrow \mathcal{L}[b_n + \sqrt{S}\sigma_n^z]\Big) \quad (2)$$

Here $\mathcal{L}[X] = X\rho X^\dagger - \frac{1}{2}(X^\dagger X\rho + \rho X^\dagger X)$. Cavity photon modes decay at loss rates κ_k, while excitons decay at rate $\Gamma_\downarrow$. The excitons are pumped by a time-dependent pulse with Gaussian envelope $P(t)$ (normalized to 1), peak amplitude $\Gamma_\uparrow$, and full-width at half-maximum (FWHM) of 2 ps. Exciton dephasing is included by rate Γ_z. Thermal relaxation and excitation of vibrons occur at rates $\gamma_\downarrow = \gamma_v(n_b + 1)$ and $\gamma_\uparrow = \gamma_v n_b$, where $n_b = \left[\exp(\omega_v/k_B T_v) - 1\right]^{-1}$ is the Bose-Einstein distribution at temperature T_v. The two-level system and relevant parameters are depicted in Fig. 1d.

Using Eq. (2) we write the equations of motion for first- and second-order correlations of the operators that contain the information of cavity mode population ($\langle a_k^\dagger a_k\rangle$) and the fraction of excited emitters ($\langle\sigma^+\sigma^-\rangle$) as functions of time. We compute the photoluminescence spectrum of the system to resolve the polariton mode energies. See Methods and Supplementary Note 4 for further details of the model.

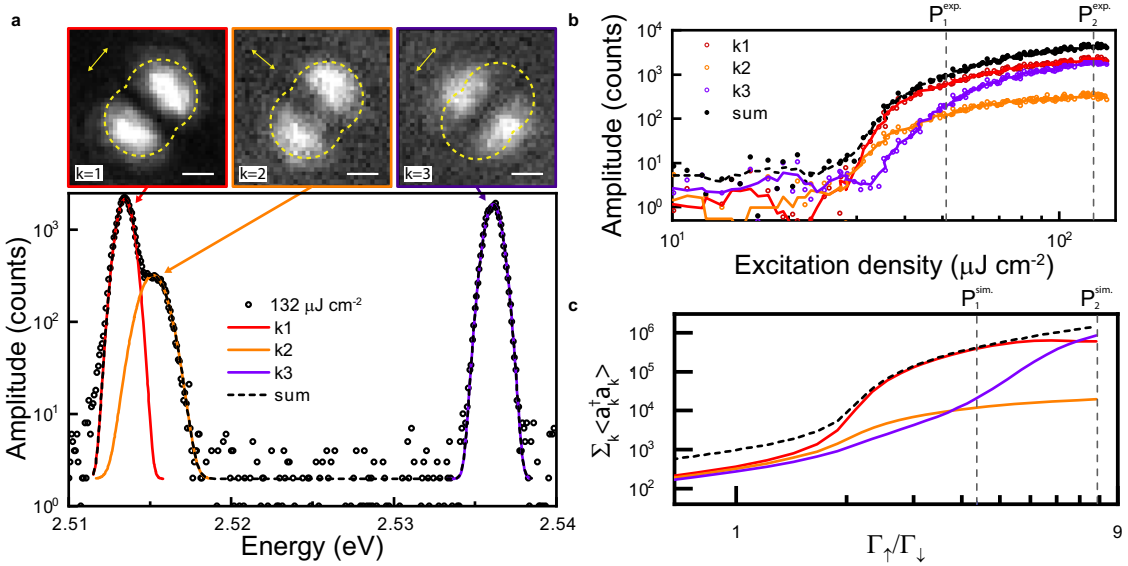

Fig. 2 | Measured and simulated multimode exciton-polariton condensates. **a** Measured emission spectrum and intensity-normalized real-space distributions of $k = 1,2,3$ modes supported by the Gaussian double-well potential at 132 μJcm^{-2} excitation fluence. See Supplementary Note 3 and Supplementary Fig. 3 for a broader emission spectrum. **b** Measured time-integrated emission intensity as a function of pump fluence for the cavity modes $k = 1,2,3$. Modes $k = 1$ and $k = 2$ are polarization split (due to birefringence of the material) with similar spatial distribution and $k = 3$ is from a different transversal order mode. Note that in general, also the mode $k = 3$ can be polarization split, however at the position on the sample where the measurements were performed, $k = 3$ polarization splitting was not observed. **c** Simulated time-integrated photon populations for the modes $k = 1,2,3$. The pump strength is given in units of $\Gamma_\uparrow/\Gamma_\downarrow$, where $\Gamma_\uparrow$ is the amplitude of the pump pulse. Dashed yellow contours and arrows in **a** depict the double-well at 3σ level and polarization of the modes, respectively. White scale bars in **a** indicate 1 μm. Dashed blue gray vertical lines in **b** and **c** depict the fluences $P_1^{\mathrm{exp.}}$ and $P_2^{\mathrm{exp.}}$ as well as $P_1^{\mathrm{sim.}}$ and $P_2^{\mathrm{sim.}}$ where autocorrelation measurements and calculations have been performed.

As revealed by the time-integrated mode populations as a function of pump strength in Fig. 2c, the mode $k = 1$ starts lasing at the lowest pump strength. With a slightly higher threshold, mode $k = 2$ is followed by $k = 3$. When the pump strength is increased, the population of mode $k = 3$ surpasses the population of mode $k = 2$ and eventually reaches equal population with mode $k = 1$. At high pump strength the two modes, $k = 1$ and $k = 3$, both have macroscopic population. The $k = 2$ mode is above its condensation threshold but with 1–2 orders of magnitude lower population.

We study the dynamics of mode populations at two pump strengths, 4 $\Gamma_\uparrow/\Gamma_\downarrow$ and 8 $\Gamma_\uparrow/\Gamma_\downarrow$, indicated by the vertical dashed lines in Fig. 2c. The pump strengths are chosen to represent approximately similar points in the threshold curve as in the experiment. Figure 3a, b show the excitation pulse (blue dashed and red dash-dotted lines) and the fraction of the excited emitters (black solid lines) as a function of time. Looking at the dynamics of the mode populations in Fig. 3c, we note that their temporal evolution follows the trend observed in the time-integrated pump strength dependence. Namely, during the rise of the excitation pulse intensity (or $\langle\sigma^+\sigma^-\rangle$) condensation in mode $k = 1$ is triggered first, as it comprises the highest population. At a higher pump strength, as shown by Fig. 3d, when $\langle\sigma^+\sigma^-\rangle$ reaches a sufficiently high value, the condensate mode switches momentarily (within 2–3 ps) from $k = 1$ to $k = 3$. When $\langle\sigma^+\sigma^-\rangle$ decreases again shortly after the peak of the pump pulse, the highest-populated mode switches back to $k = 1$. In Supplementary Note 5 and Supplementary Fig. 4 we present the results for different excitation pulse durations, showing that the switching time depends linearly on excitation pulse duration. Polariton condensation is triggered at values of $\langle\sigma^+\sigma^-\rangle$ below total inversion, as shown in Fig. 3a, b. While $\langle\sigma^+\sigma^-\rangle = 1$ would correspond to fully inverted material, lasing can generally occur at values above 0.5[29].

Mode switching signatures from simulations and experiment

Due to the limited time/spectral resolution of streak cameras, it is not possible to directly measure the dynamics at the required temporal and spectral resolution. To nevertheless address the expected temporal mode switching, we choose a different method: We calculate the intensity autocorrelation of mode populations from the simulations and study the first-order temporal coherence of the condensate in the experiment using a Michelson interferometer. First, from the simulation results we find that intensity autocorrelation of the population dynamics leads to sidelobes that could be taken as a tell-tale signature of switching. The mode populations as a function of time are self-convoluted to obtain an intensity autocorrelation function of each mode. Intensity autocorrelation of the continuous-time signal at time delay τ is given by

$$A(\tau) = \int_{-\infty}^{\infty} I(t+\tau)I(t)\mathrm{d}t. \quad (3)$$

The intensity autocorrelation functions for the two selected pump strengths are shown in Fig. 4a, b. Whereas temporal intensity profiles with a single peak lead to autocorrelation functions that peak only at $\tau = 0$, temporal profiles that have two or more peaks gives rise to sidelobes at $\tau \neq 0$.

Experimentally we study the first-order correlation by coupling the polariton emission of spectrally filtered modes into the Michelson interferometer (see Supplementary Note 6 and Supplementary Fig. 5 for details). The emission is split by a non-polarizing beam splitter cube and coupled into two interferometer arms, where one is spatially inverted and can be delayed with respect to the other. Then real-space images from both arms are overlapped and focused on a camera, resulting in an interferogram with superimposed fringes. We obtain the temporal first-order coherence from the fringe contrast as a function of interferometer arm delay by Fourier transformation of the interferograms. As we are regarding the individual modes separately due to spectral filtering and the fact that each of the respective mode profiles is point-symmetric, the spatial inversion does not yield any additional information about the spatial extension of the coherence. Below and above the threshold we expect 10 fs and 2 ps polariton coherence times, respectively. Below threshold mainly the photoluminescence signal filtered through the cavity is available due to low signal of polaritons, resulting in 10 fs coherence time. Above threshold the lifetime of the condensate is defined by the duration of the pump laser pulse, leading to 2 ps coherence time. In Fig. 4c, d we report six interferograms observed for

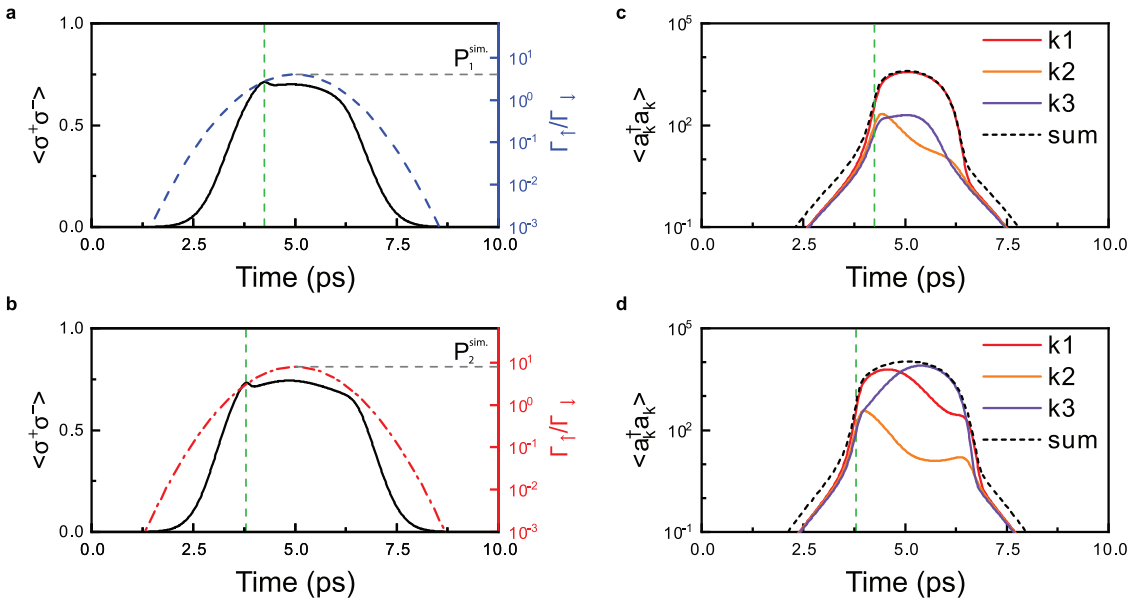

Fig. 3 | Simulated dynamics of multimode exciton-polariton condensation. **a** Fraction of excited emitters $\langle\sigma^+\sigma^-\rangle$ versus time at lower ($P_1^{\mathrm{sim.}}$) and (**b**) higher power ($P_2^{\mathrm{sim.}}$ in Fig. 2c). The dashed blue and dot-dashed red parabolic lines denote the pump pulse with Gaussian temporal envelope. The right axes show the pump strength $\Gamma_\uparrow/\Gamma_\downarrow$. **c** Occupation of modes $k = 1,2,3$ versus time at lower and (**d**) higher power. In all panels, the dashed green vertical lines depict the onset of condensation. In **a** and **b** dashed gray lines depict the $P_1^{\mathrm{sim.}}$ and $P_2^{\mathrm{sim.}}$ excitation fluences.

$k = 1, 2, 3$ at excitation fluences of $P_1^{\mathrm{exp.}} = 51\,\mu\mathrm{Jcm}^{-2}$ and at $P_1^{\mathrm{exp.}} = 123\,\mu\mathrm{Jcm}^{-2}$, respectively. At 51 μJcm^{-2}, $k = 1$ and $k = 3$ modes show the expected Gaussian-shaped correlation function, however the $k = 2$ mode's coherence shows pronounced oscillations, having a period of ~2 ps. At 123 μJcm^{-2}, $k = 1$ mode does not have the Gaussian-shaped autocorrelation function, and $k = 3$ mode shows pronounced oscillations. We underline that observing such sidelobes in the temporal coherence is a signature of temporal mode switching in the output emission of the multimode polariton condensate.

We note that intensity autocorrelation does not directly correspond to the temporal coherence measurements presented in Fig. 4c, d, as the temporal intensity profile of a pulse is not necessarily equal to its temporal coherence. The model does not provide information about how the coherence of the modes evolves as a function of time, but only about the mode occupation. It is possible that there are differences in the temporal coherence of the different modes, which can also lead to some discrepancy between model and experiment. Moreover, in the experiment there might be emission that comes not from condensed polaritons but from uncoupled or dark states that lack a well defined k-vector. Nevertheless, the calculated autocorrelation functions provide a good indication of the kind of qualitative experimental signature the temporally varying mode populations can lead to. Observing sidelobes in the measured temporal coherence suggests that mode competition is well represented in the simulations. In addition, we note that the polarization and the real-space profiles of the modes are not addressed in the model. The latter might explain the discrepancies between the simulation and experiment for the $k = 3$ mode in Fig. 2b, c as well as Fig. 4b–d .

In the future, the analysis could be extended to measurements of second-order temporal coherence to probe photon statistics and correlations between different modes, as has been done with lasers in the weak coupling regime[30–32]. However necessarily, the time resolution of such techniques has to be significantly increased in order to resolve the sub-picosecond dynamics of organic polariton condensates.

Conclusions

We have experimentally demonstrated temporal mode competition in organic multimode polariton condensates. We described the system using a beyond-mean field cumulant model that can capture the strong coupling dynamics of the photon modes and the organic emitters. Although multiple experimental parameters such as mode profiles, polarization of the modes, and precise features of the pump pulse are not included in the model, it captures and explains the experimentally observed dynamics.

Our studies introduce important perspectives on the formation of multimode organic polariton lasing and condensation and pave the way to novel types of optical oscillators and logic gates, where the condensate mode is for example switched reversibly on the picosecond time scale (THz-rate) using different modes supported by the same cavity. Moreover, our work shows how to experimentally access the multi-mode dynamics of polariton systems, including lattice Hamiltonians that can be realized by extending from a double well to multiple wells.

Methods

Fabrication

The tunable microcavity is made of two separate halves. The lower part consists of a fused silica substrate that is covered with a Distributed Bragg Reflector (DBR) comprising 9.5 layer pairs of Ta_2O_5/SiO_2 quarter-wave layers with a stop-band center at 475 nm and a 50 nm spacer layer of SiO_2 deposited with ion beam deposition. Then, a 35 nm-thin layer is spin-coated from a solution of 1% w.t. of methyl-substituted ladder-type poly(p-phenylene) (MeLPPP) dissolved in toluene. To prevent photo-induced degradation, exposure to ambient conditions and sticking of material when the cavity halves come in contact, 10 nm of SiO_2 is added by electron beam evaporation. The upper part consists of a borosilicate substrate that is etched ~30 μm deep using concentrated HF and a circular mask, forming a 200 μm diameter mesa. Gaussian-shaped double-defects (~30 nm deep, ~1000 nm full-width at halfmaximum (FWHM), 1000 nm center-to-center distance) are patterned by focused ion beam milling. Subsequently, 6.5 DBR layer pairs of Ta_2O_5/SiO_2 quarter-wave layers are deposited with ion beam deposition.

Characterization

Each cavity half is mounted on a XYZ nanopositioning stage, allowing nanometer control of the positions, at ambient conditions. The smaller stage for the top half is mounted on the stage for the bottom half. Both halves have additional control of their relative tilt angles. The bottom stage is mounted on an optical table with active mechanical vibration cancellation

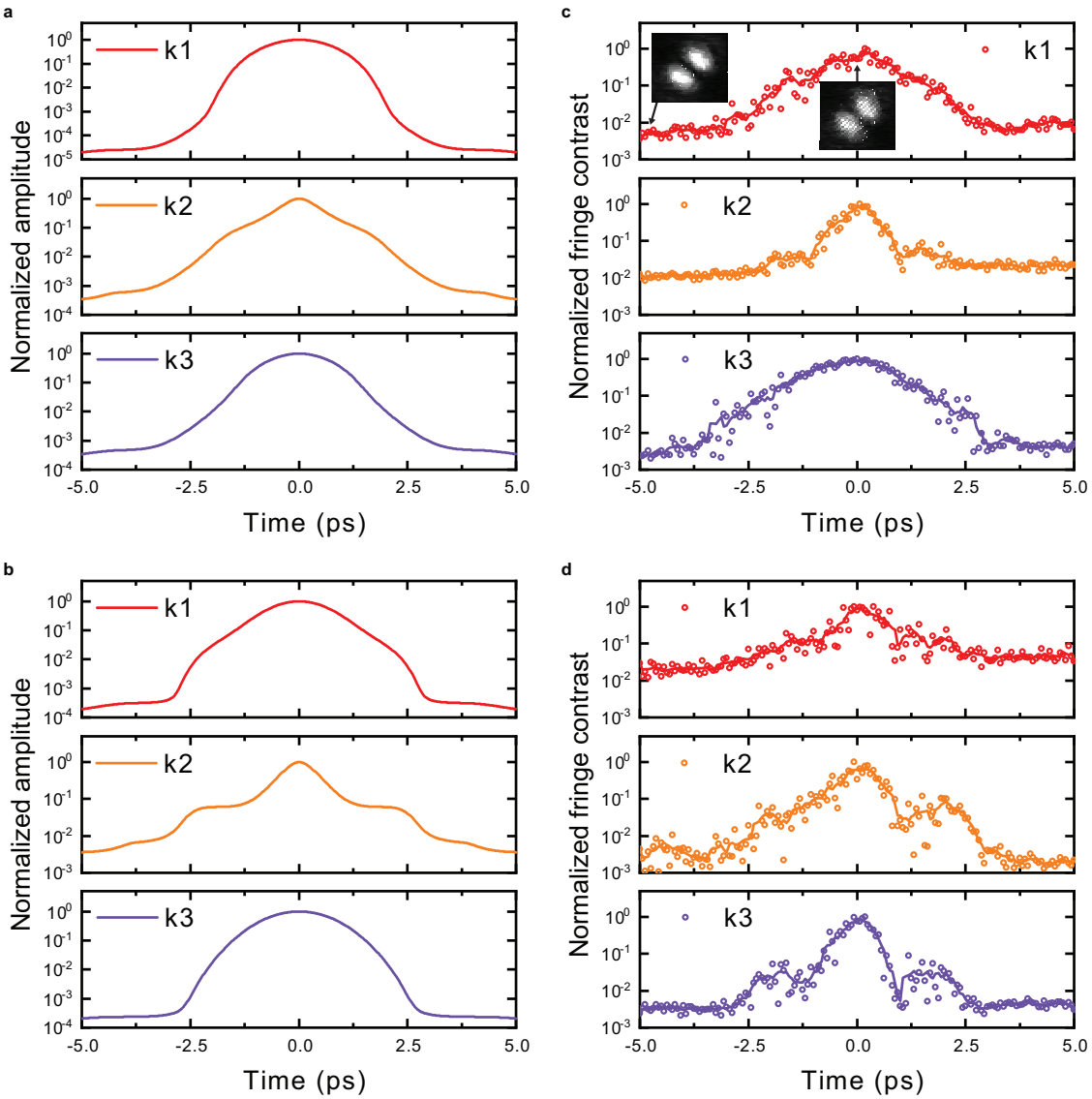

Fig. 4 | Measured temporal coherence and computed autocorrelation of photon populations. a, **b** Autocorrelation functions computed from the simulation results at low (**a**) and high (**b**) pump power. **c**, **d** Measured contrast of the interference fringes for the $k = 1,2,3$ modes above threshold at excitation density of 51 μJcm^{-2} (**c**) and 123 μJcm^{-2} (**d**). The solid lines are moving averages of 5 data points in order to smooth the noisy curves and make the sidelobes better visible. All graphs are normalized to 1.

(TableStable TS-300, actively canceling frequencies below 300 Hz). To excite the system into the polariton condensate regime, we couple a frequency-doubled regenerative amplifier, seeded by a mode-locked Ti:sapphire laser, laser at 400 nm with 1 kHz repetition rate and ~150 fs pulse duration into a multimode fiber with 25 μm core radius and 0.1 numerical aperture (NA). Transmission through the fiber stretches the pulse to 2–4 ps FWHM, as measured with a Michelson interferometer. The pump intensity at the fiber output is controlled with a movable gradient filter. We use a 100x (0.5 NA) apochromatic long working-distance microscope objective to achieve a Gaussian excitation spot with 10 μm FWHM. The emitted light is collected from the other side through the lower cavity half with a 20x objective. The spectral measurements are done by focusing the real-space image onto the entrance slit of a 0.5 m long monochromator (equipped with gratings with 300 and 1800 lines per mm) with attached cooled, back-illuminated charge coupled device (CCD) camera. Real-space images are recorded by focusing the emitted light onto another cooled CCD camera, in front of which optionally a Michelson interferometer with adjustable path length difference and retroreflector can be placed to measure the coherence. To separate the modes we use a polarizer and two angle-tunable bandpass filters (bandwidth 15 nm FWHM, Semrock VersaChrome) in series to effectively achieve 5 meV spectral width with steep edges in the detection path. See Supplementary Note 6 and Supplementary Fig. 5 for schematics of the experimental setups.

Second-order cumulant equation model

From Eq. (2) we proceed by making a basis change such that the operators σ and b are described by a generalized $N_v \times N_v$ Gell-Mann matrix basis[33] denoted as $\lambda_i^{(n)}$. In this work we include one vibrational level for each electronic level, therefore $N_v = 2$. Then we write the equations of motion up to first- and second-order correlation terms of $\lambda_i^{(n)}, a_k, a_k^\dagger$. Higher-order correlations are split into products of first- and second-order correlations, assuming third-order cumulants (e.g. $\langle ABC\rangle_c$) to be zero. From the second-order cumulant equations we obtain the temporal evolution of the number of photons in modes k, $\langle a_k^\dagger a_k\rangle$, and the fraction of the excited emitters, $\langle \sigma^+\sigma^-\rangle$. See Supplementary Note 4 for further details of the model derivation.

Simulation parameters are presented in Table 1. Parameters related to the emitters are found by matching computed absorption and emission

Table 1 | Simulation parameters

Parameter	Value
N_m	10^5
N_v	2
N_{ph}	4
ε	2.70 eV
Ω_R	0.2 eV
ω_v	0.125 eV
S	0.3
$k_B T_v$	25 meV
$1/\kappa$	85 fs
κ_0	2κ
κ_1	κ
κ_2	1.06κ
κ_3	0.995κ
$\Gamma_\downarrow$	$\frac{1}{\tau_{rad}} + \frac{1}{\tau_{nonrad}}$
τ_{rad}	310 ps
τ_{nonrad}	250 fs
$1/\Gamma_z$	250 fs
γ_v	140 fs

spectra, obtained by considering only the terms of the Hamiltonian that describe the emitters, with the experimentally measured ones. Photon mode energies are chosen such that the energies of polariton modes, obtained by computing the photoluminescence spectrum of the coupled system at very low pump strength, match with the polariton mode energies measured in the experiment. We note that the model assumes homogeneous spatial profiles of the modes. Likewise, polarization is not taken into account. These effects are captured effectively by tuning the cavity loss rate κ_k individually for each mode.

Data availability

The data that support the findings of this study are available from the corresponding author upon reasonable request.

Received: 19 September 2023; Accepted: 21 May 2024;
Published online: 22 June 2024

References

1. Carusotto, I. & Ciuti, C. Quantum fluids of light. *Rev. Mod. Phys.* **85**, 299–366 (2013).
2. Deng, H., Haug, H. & Yamamoto, Y. Exciton-polariton Bose-Einstein condensation. *Rev. Mod. Phys.* **82**, 1489–1537 (2010).
3. Keeling, J. & Kena-Cohen, S. Bose-einstein condensation of exciton-polaritons in organic microcavities. *Annu. Rev. Phys. Chem.* **71**, 435–459 (2020).
4. Plumhof, J. D., Stöferle, T., Mai, L., Scherf, U. & Mahrt, R. F. Room-temperature Bose-Einstein condensation of cavity exciton-polaritons in a polymer. *Nat. Mater.* **13**, 247 (2014).
5. Caputo, D. et al. Topological order and thermal equilibrium in polariton condensates. *Nat. Mater.* **17**, 145–151 (2018).
6. Väkeväinen, A. I. et al. Sub-picosecond thermalization dynamics in condensation of strongly coupled lattice plasmons. *Nat. Commun.* **11**, 3139 (2020).
7. Fraser, M. D., Höfling, S. & Yamamoto, Y. Physics and applications of exciton-polariton lasers. *Nat. Mater.* **15**, 1049–1052 (2016).
8. Saba, M. et al. High-temperature ultrafast polariton parametric amplification in semiconductor microcavities. *Nature* **414**, 731–735 (2001).
9. Savvidis, P. G. et al. Angle-resonant stimulated polariton amplifier. *Phys. Rev. Lett.* **84**, 1547–1550 (2000).
10. Ballarini, D. et al. All-optical polariton transistor. *Nat. Commun.* **4**, 1–8 (2013).
11. Gao, T. et al. Polariton condensate transistor switch. *Phys. Rev. B* **85**, 235102 (2012).
12. Amo, A. et al. Exciton-polariton spin switches. *Nat. Photon.* **4**, 361–366 (2010).
13. Sturm, C. et al. All-optical phase modulation in a cavity-polariton Mach-Zehnder interferometer. *Nat. Commun.* **5**, 1–7 (2014).
14. Zasedatelev, A. V. et al. A room-temperature organic polariton transistor. *Nat. Photon.* **13**, 378–383 (2019).
15. Sasikala, V. & Chitra, K. All optical switching and associated technologies: a review. *J. Opt.* **47**, 307–317 (2018).
16. Taghinejad, M. & Cai, W. All-optical control of light in micro- and nanophotonics. *ACS Photon.* **6**, 1082–1093 (2019).
17. Kang, L. et al. Nonlinear chiral meta-mirrors: enabling technology for ultrafast switching of light polarization. *Nano Lett.* **20**, 2047–2055 (2020).
18. Wang, K. et al. High contrast, femtosecond light polarization manipulation in epsilon-near-zero material coupled to a plasmonic nanoantenna array. *ACS Photon.* **8**, 2791–2799 (2021).
19. Sun, Y. et al. Stable switching among high-order modes in polariton condensates. *Phys. Rev. B* **97**, 045303 (2018).
20. Töpfer, J. D., Sigurdsson, H., Alyatkin, S. & Lagoudakis, P. G. Lotka-volterra population dynamics in coherent and tunable oscillators of trapped polariton condensates. *Phys. Rev. B* **102**, 195428 (2020).
21. Tan, E. Z., Sigurdsson, H. & Liew, T. C. H. Parity bifurcations in trapped multistable phase locked exciton-polariton condensates. *Phys. Rev. B* **97**, 075305 (2018).
22. Kim, S. et al. Coherent polariton laser. *Phys. Rev. X* **6**, 011026 (2016).
23. Maragkou, M. et al. Spontaneous nonground state polariton condensation in pillar microcavities. *Phys. Rev. B* **81**, 081307 (2010).
24. Arnardottir, K. B., Moilanen, A. J., Strashko, A., Törmä, P. & Keeling, J. Multimode organic polariton lasing. *Phys. Rev. Lett.* **125**, 233603 (2020).
25. Moilanen, A. J., Arnardóttir, K. B., Keeling, J. & Törmä, P. Mode switching dynamics in organic polariton lasing. *Phys. Rev. B* **106**, 195403 (2022).
26. Urbonas, D., Stöferle, T., Scafirimuto, F., Scherf, U. & Mahrt, R. F. Zero-dimensional organic exciton-polaritons in tunable coupled gaussian defect microcavities at room temperature. *ACS Photon.* **3**, 1542–1545 (2016).
27. Ćwik, J. A., Reja, S., Littlewood, P. B. & Keeling, J. Polariton condensation with saturable molecules dressed by vibrational modes. *Eur. Lett.* **105**, 47009 (2014).
28. Strashko, A., Kirton, P. & Keeling, J. Organic polariton lasing and the weak to strong coupling crossover. *Phys. Rev. Lett.* **121**, 193601 (2018).
29. Imamoglu, A., Ram, R. J., Pau, S. & Yamamoto, Y. Nonequilibrium condensates and lasers without inversion: Exciton-polariton lasers. *Phys. Rev. A* **53**, 4250–4253 (1996).
30. Leymann, H. A. M. et al. Intensity fluctuations in bimodal micropillar lasers enhanced by quantum-dot gain competition. *Phys. Rev. A* **87**, 053819 (2013).
31. Redlich, C. et al. Mode-switching induced super-thermal bunching in quantum-dot microlasers. *N. J. Phys.* **18**, 063011 (2016).
32. Schmidt, M. et al. Bimodal behavior of microlasers investigated with a two-channel photon-number-resolving transition-edge sensor system. *Phys. Rev. Res.* **3**, 013263 (2021).
33. Stone, M. & Goldbart, P. *Mathematics For Physics: A Guided Tour For Graduate Students* (Cambridge University Press, 2009).

Acknowledgements

We thank Dr. Jonathan Keeling for valuable discussions and comments on the manuscript. This work was supported by the Academy of Finland under

project numbers 303351, 307419, 327293, 318987 (QuantERA project RouTe), and 318937 (PROFI), as well as QuantERA project RouTe (SNSF Grant No. 20QT21_175389), and by European H2020-FETOPEN project POLLOC (Grant No. 899141). Triton cluster at Aalto University (Science-IT) was used for computations. This article is based on work from COST Action MP1403 Nanoscale Quantum Optics, supported by COST (European Cooperation in Science and Technology). Experimental part of the research was performed at the IBM Research. A.J.M. acknowledges financial support by the Jenny and Antti Wihuri Foundation, the Finnish Foundation for Technology Promotion, the Emil Aaltonen Foundation, and ETH Zürich Postdoctoral Fellowship. K.B.A. acknowledges support from EPSRC (EP/T014032/1).

Author contributions

A.J.M., D.U., and T.S. conceived the project. D.U. fabricated the samples and performed the optical measurements. A.J.M. performed the simulations with the model K.B.A. and A.J.M. developed. D.U. and A.J.M. analyzed the data and discussed the results with all other authors. U.S. synthesized the polymer. T.S., P.T., and R.F.M. supervised the project. D.U. and A.J.M. wrote the manuscript with input from all other authors.

Competing interests

The authors declare no competing interests.

Additional information

Supplementary information The online version contains supplementary material available at https://doi.org/10.1038/s42005-024-01667-w.

Correspondence and requests for materials should be addressed to Darius Urbonas or Antti J. Moilanen.

Peer review information *Communications Physics* thanks the anonymous reviewers for their contribution to the peer review of this work. A peer review file is available.